ACS APPLIED MATERIALS & INTERFACES

Research Article

Cite This: ACS Appl. Mater. Interfaces 2019, 11, 18517−18527

www.acsami.org

Tunable Thermal Energy Transport across Diamond Membranes and Diamond−Si Interfaces by Nanoscale Graphoepitaxy

Zhe Cheng,[†] Tingyu Bai,[‡] Jingjing Shi,[†] Tianli Feng,[§,∥] Yekan Wang,[‡] Matthew Mecklenburg,[⊥] Chao Li,[‡] Karl D. Hobart,[*,#] Tatyana I. Feygelson,[#] Marko J. Tadjer,[#] Bradford B. Pate,[#] Brian M. Foley,[†] Luke Yates,[†] Sokrates T. Pantelides,[§,∥] Baratunde A. Cola,[†,¶] Mark Goorsky,[‡] and Samuel Graham[*,†,¶]

[†]George W. Woodruff School of Mechanical Engineering and [¶]School of Materials Science and Engineering, Georgia Institute of Technology, Atlanta, Georgia 30332, United States

[‡]Materials Science and Engineering, University of California, Los Angeles, Los Angeles, California 91355, United States

[§]Department of Physics and Astronomy and Department of Electrical Engineering and Computer Science, Vanderbilt University, Nashville, Tennessee 37235, United States

[∥]Materials Science and Technology Division, Oak Ridge National Laboratory, Oak Ridge, Tennessee 37831, United States

[⊥]Core Center of Excellence in Nano Imaging (CNI), University of Southern California, Los Angeles, California 90089, United States

[#]U.S. Naval Research Laboratory, 4555 Overlook Ave SW, Washington, District of Columbia 20375, United States

Supporting Information

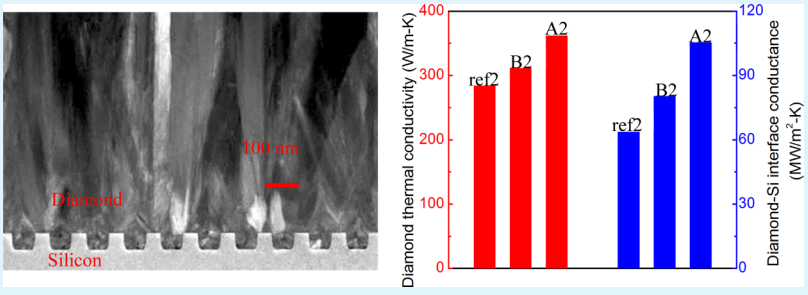

ABSTRACT: The development of electronic devices, especially those that involve heterogeneous integration of materials, has led to increased challenges in addressing their thermal operational temperature demands. The heat flow in these systems is significantly influenced or even dominated by thermal boundary resistance at the interface between dissimilar materials. However, controlling and tuning heat transport across an interface and in the adjacent materials has so far drawn limited attention. In this work, we grow chemical vapor-deposited diamond on silicon substrates by graphoepitaxy and experimentally demonstrate tunable thermal transport across diamond membranes and diamond−silicon interfaces. We observed the highest diamond−silicon thermal boundary conductance (TBC) measured to date and increased diamond thermal conductivity due to strong grain texturing in the diamond near the interface. Additionally, nonequilibrium molecular dynamics simulations and a Landauer approach are used to understand the diamond−silicon TBC. These findings pave the way for tuning or increasing thermal conductance in heterogeneously integrated electronics that involve polycrystalline materials and will impact applications including electronics thermal management and diamond growth.

KEYWORDS: *tunable thermal transport, CVD diamond, thermal boundary conductance, nanoscale graphoepitaxy, grain texturing*

1. INTRODUCTION

The ongoing miniaturization of microelectronic devices, as well as their heterogeneous integration to create advanced functionalities, has led to high local power densities and circumstances where thermal effects limit the overall device performance.[1−3] Keeping these devices cool has become a design challenge aiming to avoid the degradation of device performance and reliability.[2,3] Because of the architecture of these electronic systems, heat dissipation can be significantly influenced or even dominated by the thermal boundary resistance found at heterointerfaces.[4,5] Previous efforts to reduce thermal boundary resistance between solids include bridging phonon spectra mismatch and enhancing interfacial bonding.[6−12] In addition, several theoretical studies show that incorporating nanostructures at the interface enlarges the interface contact area and increases the thermal boundary

Received: February 2, 2019
Accepted: May 1, 2019
Published: May 1, 2019

DOI: 10.1021/acsami.9b02234
ACS Appl. Mater. Interfaces 2019, 11, 18517−18527

conductance (TBC), but experimental results are inconsistent.[13−17] Tuning thermal transport across interfaces or even in the adjacent materials remains largely an open issue.

Graphoepitaxy is a technique that uses artificial surface relief structures to induce crystallographic orientation in thin films grown on a surface.[18−21] This technique was invented to grow Si, Ge, and KCl on amorphous SiO_2 substrates about 4 decades ago.[18−21] After that, it was extensively used to grow block copolymers and carbon nanotubes to control orientation or alignment.[22−24] By introducing nanoscale graphoepitaxy into thermal transport across interfaces, the solid−solid interface contact area increases due to the artificial surface structures, which may contribute to increasing TBC. The crystallographic orientation of grains in the adjacent membranes may affect their thermal conductivity as well. These two synergistic effects provide a possible solution to tune thermal transport across interfaces and in the adjacent membranes.

In this work, we successfully grow diamond membranes on silicon substrates by nanoscale graphoepitaxy. Time domain thermoreflectance (TDTR) is used to measure the thermal conductivity of the diamond layer and the diamond−silicon TBC. The diamond thermal conductivity and diamond−silicon TBC are tuned with different surface pattern sizes. Scanning transmission electron microscopy (STEM) and X-ray diffraction (XRD) are used to study the grain size distribution and orientation. Nonequilibrium molecular dynamics (NEMD) simulation and a Landauer approach are used to understand the diamond−silicon TBC. Our work is notably the first effort to tune diamond growth on silicon substrates and subsequently thermal transport across diamond−silicon interfaces and diamond membranes by graphoepitaxy. We expect that graphoepitaxy can be applied to polycrystalline diamond grown on other substrates as well.

2. SAMPLES AND METHODOLOGIES

2.1. Samples. In this work, six silicon wafers are prepared (samples A1, B1, ref1, and A2, B2, ref2). Samples A1, A2, B1, and B2 are patterned silicon wafers with nanoscale trenches while samples ref1 and ref2 are flat silicon wafers without nanoscale trenches. The dimensions of the interface patterns are summarized in Table 1. For example, scanning electron microscopy (SEM) images of the patterned Si trenches of sample A2 are shown in Figure S1. Nanocrystalline diamond (NCD) films were fabricated with the same growth conditions on both nanopatterned and flat silicon substrates acquired from LightSmyth Technologies. NCD was grown on a flat (100) oriented polished silicon substrate by a microwave plasma-assisted chemical vapor deposition method in an IPLAS 5.0 KW CVD reactor with hydrogen and methane as reactant gases. The growth conditions were consistent throughout the entire deposition process as follows: 750 °C substrate temperature, 7.0 Torr chamber pressure, 1400 W microwave power, and 0.5% methane to hydrogen ratio. The flat Si substrate enables in situ NCD film thickness measurement using laser reflectometry and also serves as a reference for the future comparison with the patterned silicon. Prior to diamond growth, all the silicon substrates were seeded by ultrasonic treatment in an ethanol-based nanodiamond suspension prepared from detonation nanodiamond powder [International Technology Center, North Carolina, USA (ITC)]. According to the manufacturer specifications, the material grade used here has a high degree of grain size homogeneity with an average particle size of 4 nm and a chemical purity in excess of 98%. The SEM analysis of the backside of a typical NCD film deposited with implementation of the abovementioned seeding method shows a uniform seed density greater than 10^{12} nuclei/cm^2. With this type of diamond nucleation, the NCD films were formed through grain coalescence and subsequent growth competition of initially random-oriented nanodiamond seeds. Only the crystals with the fastest growth speed along the thickness direction extend to the surface. This process ultimately leads to a formation of a well-pronounced columnar grain structure in the film as well as an increase in lateral grain size with film thickness. The use of carbon-lean growth conditions as mentioned above is intended to suppress secondary renucleation and increases film quality by reducing grain boundaries.

Table 1. Dimensions of Si Patterns for Samples A, B, and ref

sample	height (nm)	top width (nm)	bottom width (nm)
A	47	60	77
B	105	205	215
ref	0	0	0

Samples A1, B1, and ref1 were used for material characterization with 1 μm-thick diamond films. Samples A2, B2, and ref2 were used for TDTR measurements with 2 μm-thick diamond films to improve TDTR sensitivity. To study the effect of nanoscale graphoepitaxy on both diamond thermal conductivity and diamond−silicon TBC on the samples, we choose the 2 μm-thick samples for thermal measurements, where TDTR is sensitive to both diamond thermal conductivity and diamond−silicon TBC. All the diamond layers were grown under the same conditions.

2.2. Thermal Characterization. The thermal properties in this work are measured by multifrequency TDTR.[25−28] TDTR is a well-established noncontact optical pump-and-probe thermal characterization tool used to measure the thermal properties of both bulk and nanostructured materials.[29,30] As shown in Figure 1, a pump beam which is chopped by a modulator heats a sample periodically and a delayed probe beam measures the temperature decay of the sample surface through a change in thermoreflectance. The probe beam delay time is controlled by a mechanical stage, which is used to create a temperature decay curve from 0.1 to 5 ns. By fitting the experimental signal picked up by a lock-in amplifier with an analytical solution of heat flow in the layered structure, one or more thermal properties of the sample can be extracted.[25−28,30,31] In TDTR measurements, the distance that the heat penetrates into the surface depends on the modulation frequency and the thermal diffusivity of the sample. By tuning the modulation frequency, we infer the thermal properties of the sample with different penetration depths, leading to different sensitivity to different unknown parameters. If we measure one spot on a sample with different modulation frequencies, we obtain TDTR data that are sensitive to more than one unknown parameters. Low-frequency TDTR measurements penetrate deeply into the samples, resulting in large sensitivity of the buried interface TBC (diamond−silicon TBC). High-frequency TDTR measurements penetrate less deeply, resulting in large sensitivity of parameters close to the sample surface (large sensitivity of diamond thermal conductivity and small sensitivity of the diamond−silicon TBC). Both frequencies have large sensitivity to Al−diamond

DOI: 10.1021/acsami.9b02234
ACS Appl. Mater. Interfaces 2019, 11, 18517−18527

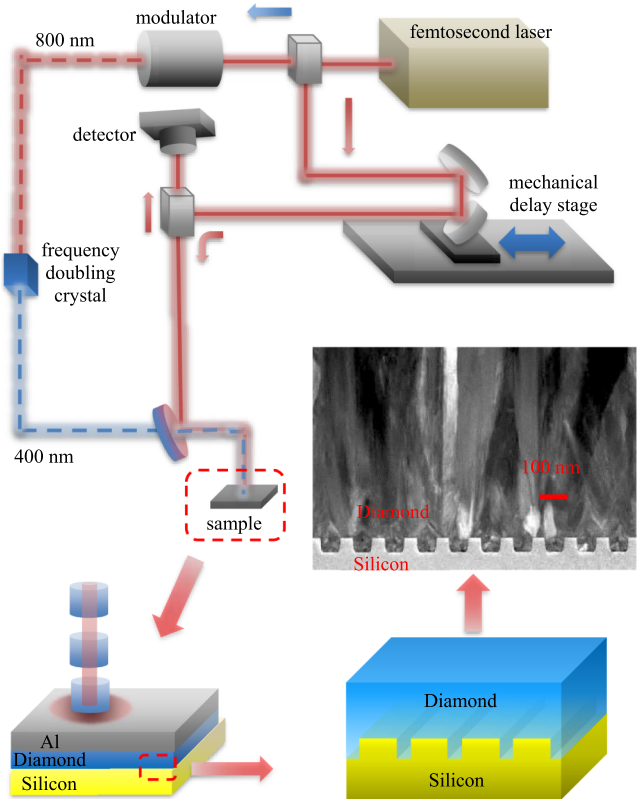

Figure 1. Schematic diagram of TDTR and sample structure grown by graphoepitaxy with nanoscale patterns. The TEM image shows the patterned diamond–silicon interface (CVD diamond grown on patterned silicon substrates by graphoepitaxy).

TBC. By fitting these TDTR curves simultaneously, we obtain the values of these unknown parameters. The definition of TDTR sensitivity is shown in eq S1 and the sensitivity analysis of the multifrequency TDTR measurements can be found in Figure S2. The sensitivity is high enough to accurately measure the unknown parameters. More details about the multi-frequency TDTR measurements can be found in our previous work and other literature.[25,27,31] The general error bars of TDTR measurements are about ±10%.

To perform TDTR measurements, a layer of aluminum (Al) is deposited on the sample surface as a transducer. The Al thicknesses are determined by the picosecond acoustic method.[32,33] In this case, we found the thickness of the Al transducer layers to be 103, 80, and 74 nm for samples A2, B2, and ref2, respectively. The thermal conductivity of the Al layer is determined by measuring its electrical conductivity and applying the Wiedemann–Franz law. The thermal conductivity of the silicon substrate is taken from the literature (142 W/m K).[34] The thickness of the diamond layers in samples A2, B2, and ref2 are measured to be 2.3 μm by SEM. The density and specific heat of CVD diamond and Al used for the analysis of the data are from the literature. The pump and probe beam size (radius) are 8.1 and 6.4 μm for samples A2 and B2, respectively. Those of sample ref2 are 7.7 and 7.5 μm, measured with a DataRay scanning slit beam profiler. A standard silicon calibration sample is checked every time before measuring the diamond samples. Three-frequency TDTR measurements are used to measure the Al–diamond TBC, diamond cross-plane thermal conductivity, and diamond–silicon TBC. As shown in Figure S2, the TDTR signal is more sensitive to diamond cross-plane thermal conductivity at high modulation frequency because heat does not penetrate through the diamond–silicon interface. The TDTR signal is more sensitive to diamond–silicon TBC at low modulation frequency because heat penetrates deep into the silicon substrate. Therefore, 1.2–3.6 or 2.2–6.3 MHz can be chosen to perform the three-frequency TDTR measurements. An example of good agreement of multifrequency TDTR data fitting of theoretical curves and experimental data is shown in Figure S3.

2.3. Materials Characterization. Plan-view and cross-sectional TEM samples were prepared using a focused ion beam microscope (Nova 600 SEM/FIB). The schematic diagram of TEM sample preparation with FIB can be found in Figure S4. The near-interface plan-view samples were made at the Si-patterned region so that both silicon and diamond can be seen. STEM images were then generated using a Titan S/TEM (FEI) system under 200 kV. The STEM mode with a high-angle annular dark field (HAADF) detector provides images with contrast because of the differences in the adjacent grain orientation. The cross-sectional STEM images were used to study the grain growth near the nucleation region. The plan-view images were used to measure the average grain size and its distribution within an area. Dark field (DF) images were also taken to show grains with either (111) or (110) plane parallel to the sample surface. These images were used to calculate the grain growth ratio for (111)- and (110)-oriented grains (more details can be found later). In order to analyze the chemical information at the interface, electron energy loss spectroscopy (EELS) was then carried out at the diamond–Si interface using JEOL JEM-2100F. XRD was used to analyze the cross-plane preferred grain orientation. The XRD 2θ:ω scan was performed on a Jordan Valley D1 diffractometer with Cu Kα_1 radiation and a parallel beam source. In these measurements, ω was offset by a few degrees from the surface orientation of the Si substrate to avoid the strong (004) Si reflection. This offset was the same for all samples, so it would not affect the measurement of the preferred orientation.

2.4. NEMD Simulations. The molecular dynamics (MD) simulations were performed using the LAMMPS[35] code and Tersoff potentials.[36] The simulation domain contains a 23 nm-long diamond (28 080 atoms) and a 33 nm-long Si (11 712 atoms) with the same cross-sectional area of 3.28 × 2.16 nm^2. The temperature difference is applied along the x direction, and periodic boundary conditions are applied along the y and z directions. In the NEMD simulations, the domains were first stabilized at 300 K by *NPT* simulations (constant pressure and temperature) with 2 000 000 steps and then converted to *NVE* (constant volume and energy) ensemble, with the temperatures of 350 and 250 K applied at the ends of diamond and Si, respectively. 3 000 000 steps of *NVE* simulations were used to stabilize the temperature gradient and heat current through the whole system. The time for each step is 0.5 fs. After that, another 2 000 000 *NVE* step simulations were performed to extract the stabilized temperature gradient and heat flux. The amorphous layer was constructed before the NEMD simulations by melting the 2 nm-long region of diamond at the interface at 3000 K with fixed volume (20% larger than crystalline diamond to allow atoms to move), followed by an annealing process to 300 K at a rate of 0.54 K/ps (10 000 000 steps) as well as an *NPT* relaxation.

2.5. Landauer Approach. The Landauer approach is a widely used method to predict TBC (G),[4,37–41] and it has been

DOI: 10.1021/acsami.9b02234
ACS Appl. Mater. Interfaces 2019, 11, 18517–18527

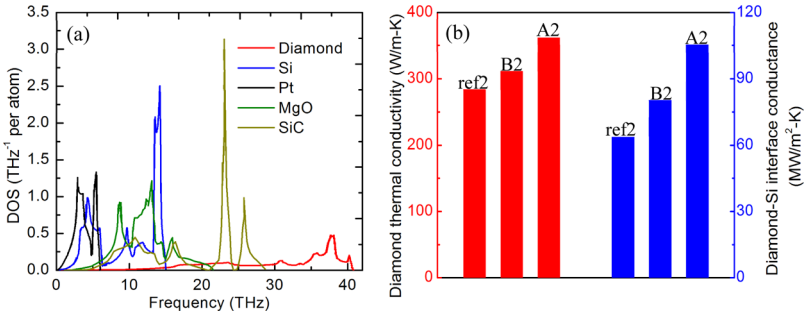

Figure 2. (a) Phonon DOS of diamond and a few other materials, highlighting the sizable differences in the vibrational spectra of different crystalline materials.[55−57] (b) Comparison of the cross-plane thermal conductivity of diamond layers and diamond−silicon TBC for the flat sample (ref2) and the patterned samples (A2 and B2).

applied here to calculate the TBC at the diamond−silicon interface. The general form of the Landauer formula calculating G at a 3D/3D interface is

$$G = \frac{q}{A\Delta T} = \frac{1}{A\Delta T}\left(\sum_p \frac{A}{2}\iint D_1(\omega) f_{BE}(T_1)\hbar\omega v_1(\omega)\tau_{12}(\theta,\omega)\cos\theta\sin\theta\,d\theta\,d\omega - \sum_p \frac{A}{2}\iint D_2(\omega) f_{BE}(T_2)\hbar\omega v_2(\omega)\tau_{21}(\theta,\omega)\cos\theta\sin\theta\,d\theta\,d\omega\right) \quad (1)$$

where q is the net heat flow rate, A is the cross-sectional area of the interface, D is the phonon density of states (DOS), f_{BE} is the Bose−Einstein distribution function, $\hbar$ is the reduced Planck constant, ω is the phonon angular frequency, v is the phonon group velocity, τ_{12} is the transmission coefficient from material 1−2 (here, it is from silicon to diamond), θ is the angle of incidence, and the sum is over all phonon modes. With the restriction of detailed balance, the formula can be simplified as

$$G = \frac{q}{A\Delta T} = \left[\sum_p \frac{1}{2}\iint D_1(\omega)(f_{BE}(T_1) - f_{BE}(T_2))\hbar\omega v_1(\omega)\tau_{12}(\theta,\omega)\cos\theta\sin\theta\,d\theta\,d\omega\right]/\Delta T \quad (2)$$

Without considering the local nonequilibrium near the interface, the formula can be further simplified as

$$G = \sum_p \frac{1}{2}\iint D_1(\omega)\frac{df_{BE}}{dT}\hbar\omega v_1(\omega)\tau_{12}(\theta,\omega)\cos\theta\sin\theta\,d\theta\,d\omega \quad (3)$$

Here, we use the diffuse mismatch model (DMM) to calculate the transmission coefficient.[38,39,41]

$$\tau_{12}(\omega) = \frac{\sum_p M_2(\omega)}{\sum_p M_1(\omega) + \sum_p M_2(\omega)} \quad (4)$$

where M is the number of modes, which is proportional to the square of the wave vector for a 3D isotropic material. The DMM assumes that all the incident phonons are diffusely scattered at the interface and lose their memory.

3. RESULTS AND DISCUSSION

3.1. Enhanced Thermal Transport Across Interfaces.

To dissipate the localized Joule heating in power electronics, CVD diamond is an excellent candidate for thermal management because of its high thermal conductivity.[42−47] However, when integrating diamond with other materials, the TBC is very small because of the large mismatch in phonon DOS between diamond and other materials. Generally speaking, phonons with a certain frequency have a high likelihood to transmit through an interface only when phonons with this frequency exist on the other side of the interface or when specific modes that are local to the interface help the transmission of those phonons.[48−53] Therefore, the degree of DOS overlap between two adjacent materials has a significant effect on the TBC across an interface. Because of the small mass of carbon atoms and strong bonds among these carbon atoms in diamond, diamond has a very high cutoff frequency (the Debye temperature of diamond is 2230 K).[54] When integrating diamond with other materials, poor DOS overlap and a correspondingly small TBC are expected. Figure 2a shows a comparison of the DOS of diamond and several typical materials (Pt, MgO, SiC, and Si). The DOS overlaps between diamond and these materials are small, leading to small TBC.[55,56]

By using multifrequency TDTR measurements,[25−28,30] we measured the diamond cross-plane thermal conductivity and the diamond−silicon TBC at room temperature and the results are shown in Figure 2b. Here, we will discuss the TBC of flat diamond−silicon interfaces first. The TBC of the flat interface in this work is measured to be 63.7 MW/m^2 K, which is very close to the value measured by Joule-heating method in the work done by Goodson et al. (about 66.7 MW/m^2 K),[58,59] larger than the value measured by 3 Ω method by Mohr et al. (50 MW/m^2 K).[60] These measured TBC of flat diamond−silicon interfaces from literature and this work are close to 60 MW/m^2 K and generally agree with each other.

In terms of theoretical calculations and simulations for diamond−silicon TBC, Khosravian et al. calculated the diamond−silicon TBC using NEMD. The TBC is determined as 335.6 MW/m^2 K, which is 5 times larger than our measured value.[61] We used NEMD to calculate the diamond−silicon TBC as well. The TBC is found to be 381 MW/m^2 K. The difference between these NEMD results derives from the difference of the used atomic potentials and size effects of finite simulation domains. The calculated TBC from the Landauer formula with transmission from DMM is 316.9 MW/m^2 K. These theoretical values calculated by NEMD and the

DOI: 10.1021/acsami.9b02234
ACS Appl. Mater. Interfaces 2019, 11, 18517−18527

Landauer approach with DMM are close to 350 MW/m^2 K and generally agree with each other while they are much larger than the experimental values. Our future work will discuss more about the fundamental understanding of diamond−silicon TBC, especially for the large difference between experimental and theoretical results.

Now we turn to our measured TBC of the nanopatterned interfaces. The measured diamond−silicon TBC for the sample grown by graphoepitaxy (sample A2) is 105 MW/m^2 K, which is the highest diamond−silicon TBC measured to date. We attribute this high measured TBC to enlarged contact area between diamond and silicon. When compared with the flat diamond−silicon interface, the diamond−silicon TBC of A2 increases by 65% for the nanopatterned interface. The patterned interface enlarges the diamond−silicon contact area, which behaves like fins in convective heat transfer. Because the fin length is very short, the relation between the ratio of the TBC and the ratio of contact area should be as below

$$\frac{G_p}{G_{ref}} \approx \frac{S_p}{S_{ref}} \quad (5)$$

Here, G_p and G_{ref}, S_p and S_{ref} are the TBC and contact areas of the patterned and reference samples. $S_p = L_t + L_b + 2h$ and $S_{ref} = L_t + L_b$. Here, L_t, L_b, and h are the top width, bottom width, and height of the pattern. The contact area of the patterned interface (samples A1 and A2) increases by 69% ($S_p/S_{ref} - 1$) compared with that of the flat diamond−silicon interface (samples ref1 and ref2). This consistency between TBC enhancement (65%) and contact area enlargement (69%) confirms that the increased TBC is due to the larger contact area. Here, we experimentally confirm the effect of increased contact area on TBC predicted by the theoretical calculations and simulation works in the literature.[13−15] For sample B2, the TBC is also enhanced by 26%, but it is smaller than the contact area enhancement (50%). This difference may be due to the grain impingement which we will discuss later, which facilitates good contact between the diamond and the side walls of the silicon patterns. For a CVD diamond near the nucleation interface, the grain size is very small. The size of the diamond seeds is only about 4 nm. Diffusive thermal transport at the diamond side is expected even if we do not consider the amorphous layer. Therefore, contact area enlargement should increase TBC. For the silicon side, the nanoscale patterns decrease the silicon thermal conductivity near the interface because of the size effect, but the dominant thermal resistance is still the diamond−silicon TBC. We acknowledge that ballistic thermal transport near the interface plays some role, but the dominant reason for the increased TBC is due to contact area enhancement. This is consistent with previous experimental and theoretical works.[13−16]

To explore the mechanism behind the enhanced thermal conductance across the interface, STEM and XRD are used to characterize the structure of the diamond−silicon interfaces. The STEM images shown in Figure 3a,b were taken using the HAADF detector to show the contrast from different grains. They show that the grains nucleating from the silicon surface tend to impinge upon one another, coalescing together in the area located above the trenches. Figure 3a shows a plan-view STEM image that includes the diamond−silicon interface and Figure 3b shows a cross-sectional STEM image of the diamond−silicon interface. We can clearly see the patterned

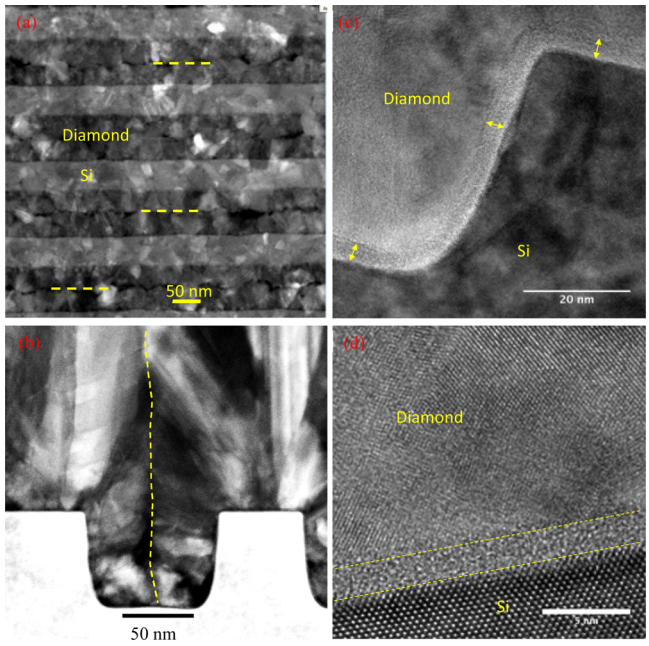

Figure 3. Grains impinge over the patterned trenches (sample A1) and amorphous layer at the diamond−silicon interface. (a) Plan-view STEM image near the diamond−silicon interface. (b) Cross-sectional STEM image of diamond−silicon interface. (c,d) Cross-sectional high-resolution transmission electron microscopy (HRTEM) images to show the amorphous carbon region at the diamond−silicon interfaces of the patterned and flat samples.

silicon ridges in Figure 3a. The diamond grains grow on the Si trench and eventually impinge at the middle of the trench region, as indicated by the yellow dashed lines shown in Figure 3a,b. This grain impingement affects the preferred crystal orientation and corresponding thermal properties. First, the grain impingement forces the grown diamond to have very good contact with the silicon nanoscale trenches. We do not observe any voids near the interface. This good contact facilitates thermal transport across the interface and enhances the TBC. This may be the reason that the TBC enhancement of sample A2 matches well with contact area enhancement. Second, the grain impingement induces preferred grain orientation (texturing) in the continually grown diamond layer.

Figure 3c,d includes HRTEM images taken at the diamond−silicon interfaces showing lattice fringes for the silicon substrate and diamond grains. As shown in Figure 3c,d, no SiC is observed at or near the interfaces for either the patterned or the flat Si−diamond interfaces. However, an amorphous layer is present (about 2 nm thick) for both interfaces. EELS is performed on the flat interface and the results are shown in Figure 4. The measurements were performed in four regions including the pure diamond region, the diamond−silicon interface region, and the silicon substrate region. The EELS results show the existence of ≤4 nm (measurement resolution) sp^2 C at the interface. The EELS measurement combined with the HRTEM image supports the conclusion that a 2 nm amorphous layer observed in the HRTEM is sp^2 C, which is formed during the diamond deposition process for both patterned and flat samples.

To study the effect of amorphous carbon at the diamond−silicon interface on thermal transport, we performed NEMD simulations. As shown in Figure 5, a temperature difference is applied across the diamond−silicon interface. We find that the

DOI: 10.1021/acsami.9b02234
ACS Appl. Mater. Interfaces 2019, 11, 18517−18527

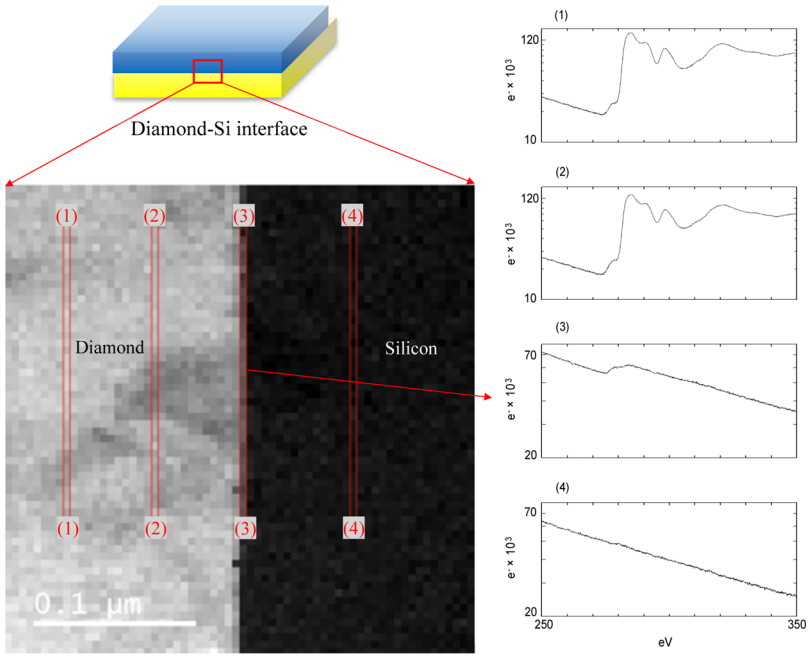

Figure 4. EELS data of diamond−silicon interface. The measurements were performed in four regions including the pure diamond region (1−2), the diamond−Si interface region (3), and the Si substrate region (4). The results show the existence of <4 nm (length of 1 pixel) sp^2 C at the interface.

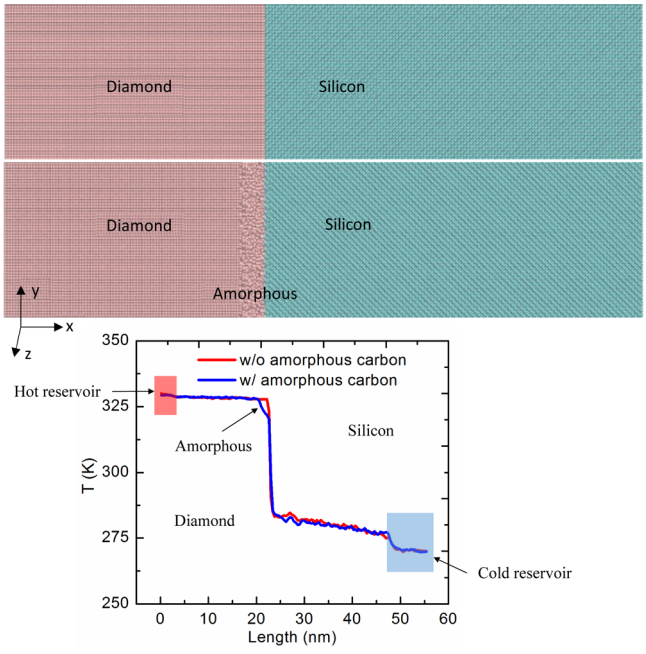

Figure 5. NEMD simulation of thermal transport across the diamond−silicon interfaces with and without amorphous carbon layer. The effect of the amorphous layer on diamond−silicon TBC is negligible (<1%).

interface between amorphous diamond and silicon presents larger thermal conductance than that between crystalline diamond and silicon, that is, the temperature jump at the interface (x = 2.2 nm) becomes smaller after the amorphous diamond layer is introduced. This is consistent with Si−Ge interfaces in the literature.[62] However, for our work, the amorphous carbon layer itself has thermal resistance that has an effect to lower the effective TBC value. Therefore, the overall interfacial thermal conductance does not change much. The overall TBC is determined as 381 MW/m^2 K without amorphous carbon and 378 MW/m^2 K with amorphous carbon for the systems, close to the previous TBC value calculated by NEMD.[61] The effect of the amorphous layer on the diamond−silicon TBC is negligible (smaller than 1%), so the intrinsic diamond−silicon thermal boundary resistance is the dominant thermal resistance at the interfaces. Moreover, this amorphous carbon layer exists for both the flat and patterned samples. Therefore, the existence of the amorphous layer does not affect our conclusion that the enhanced thermal transport across the diamond−silicon interface grown by graphoepitaxy is due to the enlarged contact area.

To understand more about the phonon mode transport across the interface, we use a Landauer approach to study the diamond−silicon TBC as well. The Landauer approach is a method in frequency space, which facilitates understanding modal phonon transport across the interface compared with NEMD. NEMD simulations include inelastic scatterings naturally from the anharmonic interatomic potentials and could model complicated interface structures, such as an amorphous layer at the interface, while the Landauer approach only considers elastic scatterings and predicts the TBC between bulk materials with perfect interfaces. The two methods provide different insights into the thermal transport across diamond−silicon interfaces, so both methods were included here.

The phonon properties of silicon and diamond are calculated from first-principles calculations. The phonon dispersion relation curves, shown in Figure 6a, are used as inputs to calculate transmission coefficients. Along the Γ-to-X direction in the reciprocal lattice, there are six phonon branches: two transverse acoustic (TA) branches, one longitudinal acoustic (LA) branch, two transverse optical branches, and one longitudinal optical branch. The phonon group velocity (the slope of the dispersion curve) of diamond is much larger than that of silicon, especially for the acoustic

DOI: 10.1021/acsami.9b02234
ACS Appl. Mater. Interfaces 2019, 11, 18517−18527

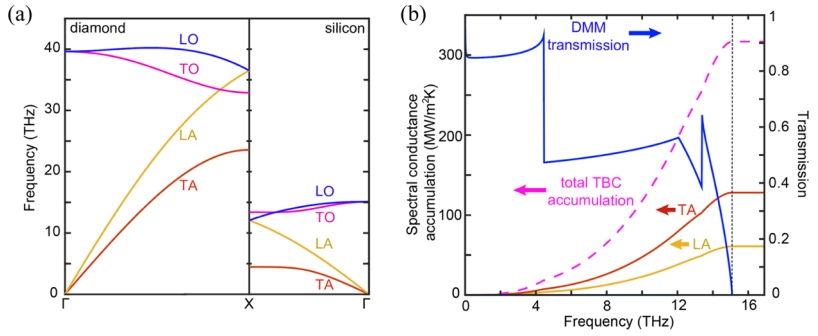

Figure 6. (a) Phonon dispersion relations of silicon and diamond from first-principles calculations. (b) Spectral conductance accumulation and the transmission coefficients from DMM at the interface between diamond and silicon. The left vertical axis is the spectral conductance accumulation while the right vertical axis is the transmission coefficient. The black dotted line is the cutoff frequency of silicon.

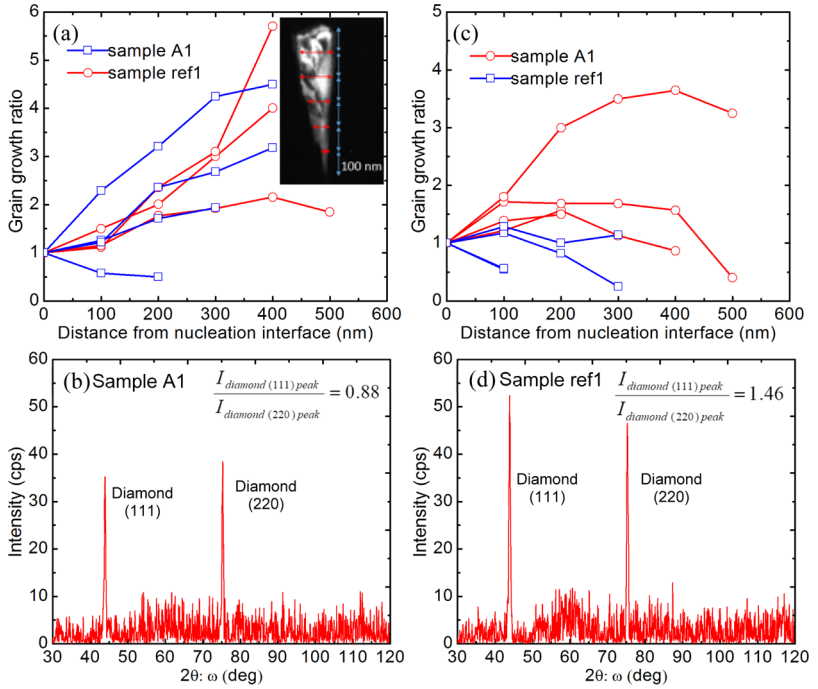

Figure 7. (a) Grain growth ratios of diamond crystals with (110) orientation. The inset (DF TEM image to select grains with (110) plane parallel to surface) shows how we measure the grain grown ratio. (b) XRD scan for sample A1. (c) Grain growth ratios of diamond crystals with (111) orientation. (d) XRD scan for sample ref1.

branches. The calculated transmission coefficients from DMM are shown in Figure 6b. In the low-frequency range (below 4.5 THz), the number of modes in silicon is much larger than that of diamond. DMM assumes that phonons lose their memory of original directions after reaching the interface. The probability of phonons propagating to the side with larger number of modes is much higher than that to the other side. As a result, the transmission coefficient at low frequency from diamond to silicon is quite high (~0.9). 4.5 THz is the cutoff frequency of the silicon TA branch. Above this frequency, the number of modes on the silicon side decreases sharply, so the transmission coefficient drops above this frequency. Here, each turning point in the transmission curve indicates the starting or cutoff frequency of a phonon branch.

The spectral conductance accumulation curve is shown in Figure 6b. For phonons with frequencies lower than 4 THz, the contribution to TBC is very small because of the small phonon DOS and small phonon energy even though the transmission coefficient is very high. For phonons with higher frequencies, the high spectral contribution to TBC results from the large phonon DOS. The contribution from TA and LA branches to TBC are calculated as well. The contribution from TA branches is twice as that from LA because TA has two branches, so the DOS is almost twice as that of LA. The TBC from Landauer is smaller than that from NEMD. We mainly attribute this difference to anharmonic contribution to TBC, which is especially true for diamond−silicon interfaces because the energy diamond phonons are much higher than the silicon phonons. It is possible that multiple silicon phonons scatter at the interface and become one diamond phonon, which contributes to transport energy across the interface (inelastic scatterings).

According to the MD simulation, the amorphous layer has negligible effect on the diamond−silicon TBC. This amorphous layer makes phonon scatterings near the interface more diffusive (closer to the assumption of DMM). However, some recent modeling results show that there exists a localized interface mode at the interface which affects thermal transport

DOI: 10.1021/acsami.9b02234
ACS Appl. Mater. Interfaces 2019, 11, 18517−18527

across the interface significantly.[51,63,64] The assumption of Landauer formula with a transmission coefficient deriving from DMM may not hold with the existence of interface mode. The diamond−silicon interface with and without an amorphous layer possibly have different interface modes. We will discuss this more in our future work. As an estimate of upper limit of diamond−silicon TBC, the radiation limit is calculated as 569 MW/m^2 K.

3.2. Enhanced Thermal Conduction in Diamond Membranes. As shown in Figure 2b, very surprisingly, we find that the diamond cross-plane thermal conductivity of the patterned samples grown by graphoepitaxy (samples A2 and B2) increases by 28 and 10% compared with that of the flat sample (sample ref2). To figure out the structure−property relation, we used TEM to study the grain sizes of the diamond layer. In polycrystalline dielectric materials, phonons dominate thermal conduction. Phonons scatter with defects, grain boundaries, and phonons, which determine phonon mean-free path and correspondingly thermal conductivity. Large grains (less boundaries) scatter phonons less extensively, leading to a long phonon mean-free path and correspondingly high thermal conductivity.[31,65,66] In order to measure the grain growth ratio for grains with different orientations, DF images were generated over several micrometer length of the TEM samples. An aperture was used to select the reciprocal lattice points in selected area diffraction patterns that correspond to grains with (111) or (110) planes parallel to the sample surface. The resulting images show the selected grains in bright contrast. As an example, a diamond grain with (110) orientation is shown in the inset of Figure 7a. The grain width (indicated with red arrows) was measured every 100 nm (indicated with blue arrows) from the depth at which the grain is first observed. We define the "grain growth ratio" as the ratio of the grain size measured at different distances over the grain size measured at 100 nm in order to quantify if grains with certain orientations grow at the expense of others. Figure 7a,c shows how the grain growth ratios of several diamond crystals with (111) orientation and (110) orientation parallel to the surface change with different distances from the nucleation interface. As depicted in Figure 7, for diamond layers grown on both patterned and flat silicon substrates (samples A1 and ref1), grains with (111) orientation typically shrink or are blocked by other grains, while grains with (110) orientation tend to expand horizontally while growing. As a result, grains with (110) orientation are longer (wider) in the film thickness (cross-plane) direction than grains with (111) orientation. Similarly, it has been reported that the (110) grain orientation is a preferred grain orientation for CVD diamond growth under certain conditions.[67−69] As discussed above, these long (wide) grains scatter phonons less extensively in the cross-plane direction, resulting in longer phonon mean-free path and correspondingly higher thermal conductivity.

To assess the cross-plane preferred grain orientation, samples A1, B1, and ref1 were measured using XRD $2\theta{:}\omega$ scans. The XRD peak intensities are from the grains that have the specific plane parallel to the surface and the integrated intensity ratio provides information about the preferred orientation. The XRD patterns of samples A1 and ref1 are shown in Figure 7b,d as a comparison. The integrated intensity ratio $I_{\text{diamond(111) peak}}/I_{\text{diamond(220) peak}}$ of samples A1, B1, and ref1 are 0.88, 1.13, and 1.46, respectively. Samples A1 and B1 have smaller integrated intensity ratio than sample ref1 (all of them are smaller than a ratio of 2.50, which would be the ratio for random grain orientations). This feature indicates that all the three samples have (110) preferred orientation while the patterned sample (A1, B1) shows stronger (110) preferred orientation than the flat sample. As discussed above, crystals with (111) orientation typically shrink or are blocked while crystals with (110) orientation are not. When compared with grains with (111) orientation, the long (wide) crystals with (110) orientation facilitate thermal conduction along the cross-plane direction because of reduced phonon grain boundary scattering.[66] The higher fraction of grains with (110) orientation in the diamond layer grown by graphoepitaxy leads to long phonon mean-free path. This result explains the high cross-plane thermal conductivity measured in patterned samples.

To further confirm our conclusions about the grain size impact, we also measured the grain distributions of samples A2 and ref2 with plan-view TEM samples as many more grains could be measured with cross sectional TEM. Figure 8a,b shows the STEM images of samples A2 and ref2 near the surfaces of the diamond layers. The grain size is measured within the yellow box in the images and the distribution information is summarized in Figure 8c. The average grain size of the patterned sample is 247 nm, which is larger than that of the flat sample (216 nm). Moreover, the patterned sample does not have very small grains (0−100 nm) and has a distribution that is weighted toward larger grain sizes (the patterned sample has 19 grains larger than 250 nm in this area while the flat sample has only 13 within the 5.8 μm^2 area). Grain boundaries scatter phonons and limit phonon mean-free paths, leading to a reduced thermal conductivity.[65,66,70] The larger average grain size and lower concentration of very small grains (less grain boundaries) scatter phonons less extensively, leading to long phonon mean-free path and high thermal conductivity, which helps explain the observation that the cross-plane thermal conductivity of the diamond grown by graphoepitaxy is higher than that grown on the flat sample.

4. CONCLUSIONS

The thermal boundary resistance can be an important factor that limits the heat flow out of high power density electronics and microelectronics that require the heterogeneous integration of materials. This is especially true for chemically deposited diamond integrated with other semiconductors because of the large phonon DOS mismatch between diamond and other materials. However, we show for the first time that it is possible to increase the TBC at semiconductor−dielectric interfaces by graphoepitaxy. By growing diamond on nano-patterned silicon wafers, the present work provides a general strategy to significantly reduce the thermal resistance of both the diamond layer and the diamond−substrate interface simultaneously. The diamond−silicon TBC increases by 65% compared with that of a flat diamond−silicon interface, which is consistent with the contact area enlargement (69%). Our results experimentally confirm the effect of contact area enlargement on TBC predicted by previous theoretical works and achieve the highest diamond−silicon TBC measured to date. The NEMD simulation results show that the amorphous carbon layer at the interface has negligible effect on thermal transport across the interface and the large intrinsic diamond−silicon thermal boundary resistance is the dominant thermal resistance. A Landauer approach is used to calculate diamond−silicon TBC and understand phonon transmissions across the interface. Furthermore, compared with that of the diamond

DOI: 10.1021/acsami.9b02234
ACS Appl. Mater. Interfaces 2019, 11, 18517−18527

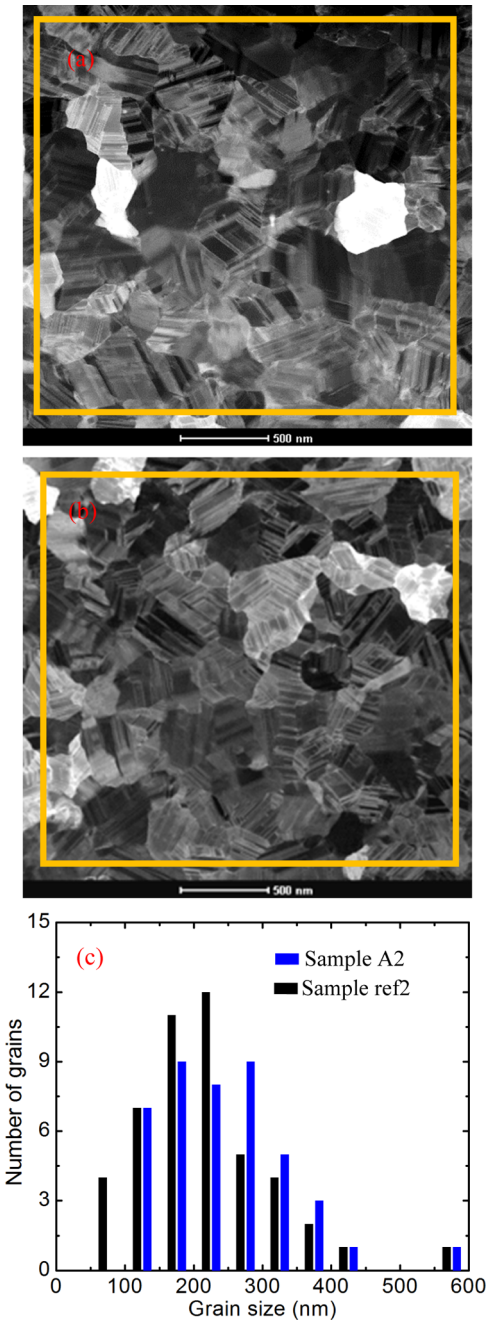

Figure 8. Plan-view STEM image near the diamond film surface for 2 μm samples: (a) patterned sample (sample A2) and (b) flat sample (sample ref2). (c) Grain distribution of samples A2 and ref2. The average grain size of sample A2 is 247 nm while that of sample ref2 is 216 nm.

layer grown on the flat silicon substrate, we observe a 28% increase in the thermal conductivity of the diamond layer grown on the patterned substrate, which is due to the preferred grain orientation (texturing) measured by STEM and XRD. In diamond layers grown on both patterned and flat silicon substrates, grains with (110) orientation typically tend to expand while growing grains with (111) orientation shrink or blocked by other grains. XRD results show that the diamond layer grown on the patterned substrate has stronger (110) texturing than that on the flat substrate. This finding is confirmed by grain distribution analysis on diamond grain sizes near the grown side for samples A2 and ref2. The average grain size of the patterned sample A2 (247 nm) is slightly larger than that of the flat sample ref2 (216 nm). Moreover, the patterned sample does not have very small grains (0−100 nm) and has a distribution that is weighted toward larger grain sizes. Graphoepitaxy provides a general solution to significantly enhance thermal transport across diamond layers and diamond−substrate interfaces when integrating diamond to substrates for applications of electronics cooling.

■ ASSOCIATED CONTENT

Supporting Information

The Supporting Information is available free of charge on the ACS Publications website at DOI: 10.1021/acsami.9b02234.

SEM pictures of nanoscale patterns, TDTR sensitivity analysis, data fitting, and TEM sample preparation instruction with FIB (PDF)

■ AUTHOR INFORMATION

Corresponding Authors

*E-mail: karl.hobart@nrl.navy.mil (K.D.H.).
*E-mail: sgraham@gatech.edu (S.G.).

ORCID

Zhe Cheng: 0000-0001-7827-2979
Jingjing Shi: 0000-0002-0249-4468
Tianli Feng: 0000-0002-7284-5657
Bradford B. Pate: 0000-0002-3288-2947
Samuel Graham: 0000-0002-1299-1636

Notes

The authors declare the following competing financial interest(s): A patent related to this work has been applied with application number 62/676,294 filed by May 25, 2018.

■ ACKNOWLEDGMENTS

The authors would like to acknowledge the funding support from the U.S. Defense Advanced Research Projects Agency (DARPA) Diamond Round Robin Program "Thermal Transport in Diamond Thin Films for Electronic Thermal Management" under contract no. FA8650-15C and ONR MURI Grant No. N00014-18-1-2429. The NEMD simulations by T.I.F. and S.T.P. are supported in part by the Department of Energy grant DE-FG0209ER46554 and the McMinn Endowment. Computations at Vanderbilt University and ORNL were performed at the National Energy Research Scientific Computing Center (NERSC), a Department of Energy, Office of Science, User Facility funded through contract no. DE-AC02-05CH11231. Computations also used the Extreme Science and Engineering Discovery Environment (XSEDE).

■ REFERENCES

(1) Cahill, D. G.; Braun, P. V.; Chen, G.; Clarke, D. R.; Fan, S.; Goodson, K. E.; Keblinski, P.; King, W. P.; Mahan, G. D.; Majumdar, A.; Maris, H. J.; Phillpot, S. R.; Pop, E.; Shi, L. Nanoscale thermal transport. II. 2003-2012. *Appl. Phys. Rev.* **2014**, *1*, 011305.
(2) Moore, A. L.; Shi, L. Emerging challenges and materials for thermal management of electronics. *Mater. Today* **2014**, *17*, 163−174.
(3) Pop, E. Energy dissipation and transport in nanoscale devices. *Nano Res.* **2010**, *3*, 147−169.
(4) Lyeo, H.-K.; Cahill, D. G. Thermal conductance of interfaces between highly dissimilar materials. *Phys. Rev. B: Condens. Matter Mater. Phys.* **2006**, *73*, 144301.

DOI: 10.1021/acsami.9b02234
ACS Appl. Mater. Interfaces 2019, 11, 18517−18527

(5) Costescu, R. M.; Wall, M. A.; Cahill, D. G. Thermal conductance of epitaxial interfaces. *Phys. Rev. B: Condens. Matter Mater. Phys.* **2003**, *67*, 054302.
(6) Majumdar, S.; Sierra-Suarez, J. A.; Schiffres, S. N.; Ong, W.-L.; Higgs, C. F., III; McGaughey, A. J. H.; Malen, J. A. Vibrational mismatch of metal leads controls thermal conductance of self-assembled monolayer junctions. *Nano Lett.* **2015**, *15*, 2985−2991.
(7) O'Brien, P. J.; Shenogin, S.; Liu, J.; Chow, P. K.; Laurencin, D.; Mutin, P. H.; Yamaguchi, M.; Keblinski, P.; Ramanath, G. Bonding-induced thermal conductance enhancement at inorganic heterointerfaces using nanomolecular monolayers. *Nat. Mater.* **2013**, *12*, 118−122.
(8) Zheng, K.; Sun, F.; Zhu, J.; Ma, Y.; Li, X.; Tang, D.; Wang, F.; Wang, X. Enhancing the thermal conductance of polymer and sapphire interface via self-assembled monolayer. *ACS Nano* **2016**, *10*, 7792−7798.
(9) Losego, M. D.; Grady, M. E.; Sottos, N. R.; Cahill, D. G.; Braun, P. V. Effects of chemical bonding on heat transport across interfaces. *Nat. Mater.* **2012**, *11*, 502−506.
(10) Collins, K. C.; Chen, S.; Chen, G. Effects of surface chemistry on thermal conductance at aluminum-diamond interfaces. *Appl. Phys. Lett.* **2010**, *97*, 083102.
(11) Sun, F.; Zhang, T.; Jobbins, M. M.; Guo, Z.; Zhang, X.; Zheng, Z.; Tang, D.; Ptasinska, S.; Luo, T. Molecular Bridge Enables Anomalous Enhancement in Thermal Transport across Hard-Soft Material Interfaces. *Adv. Mater.* **2014**, *26*, 6093−6099.
(12) Zhou, Y.; Anaya, J.; Pomeroy, J.; Sun, H.; Gu, X.; Xie, A.; Beam, E.; Becker, M.; Grotjohn, T. A.; Lee, C.; Kuball, M. Barrier-Layer Optimization for Enhanced GaN-on-Diamond Device Cooling. *ACS Appl. Mater. Interfaces* **2017**, *9*, 34416−34422.
(13) Hu, M.; Zhang, X.; Poulikakos, D.; Grigoropoulos, C. P. Large "near junction" thermal resistance reduction in electronics by interface nanoengineering. *Int. J. Heat Mass Transfer* **2011**, *54*, 5183−5191.
(14) Zhou, X. W.; Jones, R. E.; Kimmer, C. J.; Duda, J. C.; Hopkins, P. E. Relationship of thermal boundary conductance to structure from an analytical model plus molecular dynamics simulations. *Phys. Rev. B: Condens. Matter Mater. Phys.* **2013**, *87*, 094303.
(15) Lee, E.; Zhang, T.; Hu, M.; Luo, T. Thermal boundary conductance enhancement using experimentally achievable nanostructured interfaces - analytical study combined with molecular dynamics simulation. *Phys. Chem. Chem. Phys.* **2016**, *18*, 16794−16801.
(16) Lee, E.; Zhang, T.; Yoo, T.; Guo, Z.; Luo, T. Nanostructures Significantly Enhance Thermal Transport across Solid Interfaces. *ACS Appl. Mater. Interfaces* **2016**, *8*, 35505−35512.
(17) Hopkins, P. E.; Duda, J. C.; Petz, C. W.; Floro, J. A. Controlling thermal conductance through quantum dot roughening at interfaces. *Phys. Rev. B: Condens. Matter Mater. Phys.* **2011**, *84*, 035438.
(18) Smith, H. I.; Flanders, D. C. Oriented crystal growth on amorphous substrates using artificial surface-relief gratings. *Appl. Phys. Lett.* **1978**, *32*, 349−350.
(19) Geis, M. W.; Tsaur, B.-Y.; Flanders, D. C. Graphoepitaxy of germanium on gratings with square-wave and sawtooth profiles. *Appl. Phys. Lett.* **1982**, *41*, 526−529.
(20) Geis, M.; Flanders, D.; Antoniadis, D.; Smith, H. *Crystalline Silicon on Insulators by Graphoepitaxy, Electron Devices Meeting*; IEEE, 1979; pp 210−212.
(21) Geis, M. W.; Flanders, D. C.; Smith, H. I. Crystallographic orientation of silicon on an amorphous substrate using an artificial surface-relief grating and laser crystallization. *Appl. Phys. Lett.* **1979**, *35*, 71−74.
(22) Segalman, R. A.; Yokoyama, H.; Kramer, E. J. Graphoepitaxy of spherical domain block copolymer films. *Adv. Mater.* **2001**, *13*, 1152−1155.
(23) Bita, I.; Yang, J. K. W.; Jung, Y. S.; Ross, C. A.; Thomas, E. L.; Berggren, K. K. Graphoepitaxy of self-assembled block copolymers on two-dimensional periodic patterned templates. *Science* **2008**, *321*, 939−943.
(24) Ismach, A.; Kantorovich, D.; Joselevich, E. Carbon nanotube graphoepitaxy: Highly oriented growth by faceted nanosteps. *J. Am. Chem. Soc.* **2005**, *127*, 11554−11555.
(25) Liu, J.; Zhu, J.; Tian, M.; Gu, X.; Schmidt, A.; Yang, R. Simultaneous measurement of thermal conductivity and heat capacity of bulk and thin film materials using frequency-dependent transient thermoreflectance method. *Rev. Sci. Instrum.* **2013**, *84*, 034902.
(26) Bougher, T. L.; Yates, L.; Lo, C.-F.; Johnson, W.; Graham, S.; Cola, B. A. Thermal boundary resistance in GaN films measured by time domain thermoreflectance with robust Monte Carlo uncertainty estimation. *Nanoscale Microscale Thermophys. Eng.* **2016**, *20*, 22−32.
(27) Jiang, P.; Huang, B.; Koh, Y. K. Accurate measurements of cross-plane thermal conductivity of thin films by dual-frequency time-domain thermoreflectance (TDTR). *Rev. Sci. Instrum.* **2016**, *87*, 075101.
(28) Cho, J.; Francis, D.; Altman, D. H.; Asheghi, M.; Goodson, K. E. Phonon conduction in GaN-diamond composite substrates. *J. Appl. Phys.* **2017**, *121*, 055105.
(29) Rougher, T. L.; Yates, L.; Cheng, Z.; Cola, B. A.; Graham, S.; Chaeito, R.; Sood, A.; Ashegi, M.; Goodson, K. E. Experimental considerations of CVD diamond film measurements using time domain thermoreflectance. *2017 16th IEEE Intersociety Conference on ITherm*; IEEE, 2017; pp 30−38.
(30) Cahill, D. G. Analysis of heat flow in layered structures for time-domain thermoreflectance. *Rev. Sci. Instrum.* **2004**, *75*, 5119−5122.
(31) Cheng, Z.; Bougher, T.; Bai, T.; Wang, S. Y.; Li, C.; Yates, L.; Foley, B. M.; Goorsky, M.; Cola, B. A.; Faili, F.; Graham, S. Probing Growth-Induced Anisotropic Thermal Transport in High-Quality CVD Diamond Membranes by Multifrequency and Multiple-Spot-Size Time-Domain Thermoreflectance. *ACS Appl. Mater. Interfaces* **2018**, *10*, 4808−4815.
(32) Hohensee, G. T.; Hsieh, W.-P.; Losego, M. D.; Cahill, D. G. Interpreting picosecond acoustics in the case of low interface stiffness. *Rev. Sci. Instrum.* **2012**, *83*, 114902.
(33) Daly, B. C.; Kang, K.; Wang, Y.; Cahill, D. G. Picosecond ultrasonic measurements of attenuation of longitudinal acoustic phonons in silicon. *Phys. Rev. B: Condens. Matter Mater. Phys.* **2009**, *80*, 174112.
(34) Asheghi, M.; Touzelbaev, M. N.; Goodson, K. E.; Leung, Y. K.; Wong, S. S. Temperature-dependent thermal conductivity of single-crystal silicon layers in SOI substrates. *J. Heat Transfer* **1998**, *120*, 30−36.
(35) Plimpton, S. Fast parallel algorithms for short-range molecular dynamics. *J. Comput. Phys.* **1995**, *117*, 1−19.
(36) Baskes, M. I.; Nelson, J. S.; Wright, A. F. Semiempirical modified embedded-atom potentials for silicon and germanium. *Phys. Rev. B: Condens. Matter Mater. Phys.* **1989**, *40*, 6085.
(37) Landauer, R. Spatial variation of currents and fields due to localized scatterers in metallic conduction. *IBM J. Res. Dev.* **1957**, *1*, 223−231.
(38) Little, W. A. The transport of heat between dissimilar solids at low temperatures. *Can. J. Phys.* **1959**, *37*, 334−349.
(39) Fisher, T. S. *Thermal Energy at the Nanoscale*; World Scientific Publishing Company, 2013; Vol. 3.
(40) Stoner, R. J.; Maris, H. J. Kapitza conductance and heat flow between solids at temperatures from 50 to 300 K. *Phys. Rev. B: Condens. Matter Mater. Phys.* **1993**, *48*, 16373.
(41) Swartz, E. T.; Pohl, R. O. Thermal boundary resistance. *Rev. Mod. Phys.* **1989**, *61*, 605.
(42) Cho, J.; Li, Z.; Bozorg-Grayeli, E.; Kodama, T.; Francis, D.; Ejeckam, F.; Faili, F.; Asheghi, M.; Goodson, K. E. Improved Thermal Interfaces of GaN-Diamond Composite Substrates for HEMT Applications. *IEEE Trans. Compon., Packag., Manuf. Technol.* **2013**, *3*, 79−85.
(43) Faili, F.; Palmer, N. L.; Oh, S.; Twitchen, D. J.. *Physical and Thermal Characterization of CVD Diamond, a Bottoms up Review*; ITherm: Orlando, Florida, US, 2017.

DOI: 10.1021/acsami.9b02234
ACS Appl. Mater. Interfaces 2019, 11, 18517−18527

(44) Yates, L.; Sood, A.; Cheng, Z.; Bougher, T.; Malcolm, K.; Cho, J.; Asheghi, M.; Goodson, K.; Goorsky, M.; Faili, F.. *Characterization of the Thermal Conductivity of CVD Diamond for GaN-on-Diamond Devices, Compound Semiconductor Integrated Circuit Symposium (CSICS), 2016 IEEE*; IEEE, 2016; pp 1−4.
(45) Anaya, J.; Bai, T.; Wang, Y.; Li, C.; Goorsky, M.; Bougher, T. L.; Yates, L.; Cheng, Z.; Graham, S.; Hobart, K. D.; Feygelson, T. I.; Tadjer, M. J.; Anderson, T. J.; Pate, B. B.; Kuball, M. Simultaneous determination of the lattice thermal conductivity and grain/grain thermal resistance in polycrystalline diamond. *Acta Mater.* **2017**, *139*, 215−225.
(46) Cheaito, R.; Sood, A.; Yates, L.; Bougher, T. L.; Cheng, Z.; Asheghi, M.; Graham, S.; Goodson, K. Thermal conductivity measurements on suspended diamond membranes using picosecond and femtosecond time-domain thermoreflectance. *2017 16th IEEE Intersociety Conference on ITherm*; IEEE, 2017; pp 706−710.
(47) Cheng, Z.; Yates, L.; Shi, J.; Tadjer, M. J.; Hobart, K. D.; Graham, S. Thermal conductance across β-Ga2O3-diamond van der Waals heterogeneous interfaces. *APL Mater.* **2019**, *7*, 031118.
(48) Giri, A.; Hopkins, P. E. Role of interfacial mode coupling of optical phonons on thermal boundary conductance. *Sci. Rep.* **2017**, *7*, 11011.
(49) Murakami, T.; Hori, T.; Shiga, T.; Shiomi, J. Probing and tuning inelastic phonon conductance across finite-thickness interface. *Appl. Phys. Express* **2014**, *7*, 121801.
(50) Gordiz, K.; Henry, A. Phonon transport at interfaces: Determining the correct modes of vibration. *J. Appl. Phys.* **2016**, *119*, 015101.
(51) Gordiz, K.; Henry, A. Phonon transport at crystalline Si/Ge interfaces: the role of interfacial modes of vibration. *Sci. Rep.* **2016**, *6*, 23139.
(52) Gaskins, J. T.; Kotsonis, G.; Giri, A.; Ju, S.; Rohskopf, A.; Wang, Y.; Bai, T.; Sachet, E.; Shelton, C. T.; Liu, Z.; Cheng, Z.; Foley, B. M.; Graham, S.; Luo, T.; Henry, A.; Goorsky, M. S.; Shiomi, J.; Maria, J.-P.; Hopkins, P. E. Thermal Boundary Conductance Across Heteroepitaxial ZnO/GaN Interfaces: Assessment of the Phonon Gas Model. *Nano Lett.* **2018**, *18*, 7469−7477.
(53) Giri, A.; King, S. W.; Lanford, W. A.; Mei, A. B.; Merrill, D.; Li, L.; Oviedo, R.; Richards, J.; Olson, D. H.; Braun, J. L.; Gaskins, J. T.; Deangelis, F.; Henry, A.; Hopkins, P. E. Interfacial Defect Vibrations Enhance Thermal Transport in Amorphous Multilayers with Ultrahigh Thermal Boundary Conductance. *Adv. Mater.* **2018**, *30*, 1804097.
(54) Kittel, C. *Introduction to Solid State Physics*; Wiley, 2005.
(55) Hohensee, G. T.; Wilson, R.; Cahill, D. G. Thermal conductance of metal−diamond interfaces at high pressure. *Nat. Commun.* **2015**, *6*, 6578.
(56) Liu, Z.-K.; Wang, Y.; Shang, S. Thermal expansion anomaly regulated by entropy. *Sci. Rep.* **2014**, *4*, 7043.
(57) Wang, Y.; Wang, J. J.; Wang, W. Y.; Mei, Z. G.; Shang, S. L.; Chen, L. Q.; Liu, Z. K. A mixed-space approach to first-principles calculations of phonon frequencies for polar materials. *J. Phys.: Condens. Matter* **2010**, *22*, 202201.
(58) Goodson, K. E.; Käding, O. W.; Rösler, M.; Zachai, R. Experimental investigation of thermal conduction normal to diamond-silicon boundaries. *J. Appl. Phys.* **1995**, *77*, 1385−1392.
(59) Goodson, K. E.; Käding, O. W.; Rösner, M.; Zachai, R. Thermal conduction normal to diamond-silicon boundaries. *Appl. Phys. Lett.* **1995**, *66*, 3134−3136.
(60) Mohr, M.; Daccache, L.; Horvat, S.; Brühne, K.; Jacob, T.; Fecht, H.-J. Influence of grain boundaries on elasticity and thermal conductivity of nanocrystalline diamond films. *Acta Mater.* **2017**, *122*, 92−98.
(61) Khosravian, N.; Samani, M. K.; Loh, G. C.; Chen, G. C. K.; Baillargeat, D.; Tay, B. K. Molecular dynamic simulation of diamond/silicon interfacial thermal conductance. *J. Appl. Phys.* **2013**, *113*, 024907.
(62) Gordiz, K.; Henry, A. Phonon transport at interfaces between different phases of silicon and germanium. *J. Appl. Phys.* **2017**, *121*, 025102.
(63) Chalopin, Y.; Volz, S. A microscopic formulation of the phonon transmission at the nanoscale. *Appl. Phys. Lett.* **2013**, *103*, 051602.
(64) Feng, T.; Zhong, Y.; Shi, J.; Ruan, X. Unexpected high inelastic phonon transport across solid-solid interface: Modal nonequilibrium molecular dynamics simulations and Landauer analysis. *Phys. Rev. B* **2019**, *99*, 045301.
(65) Anaya, J.; Rossi, S.; Alomari, M.; Kohn, E.; Tóth, L.; Pécz, B.; Hobart, K. D.; Anderson, T. J.; Feygelson, T. I.; Pate, B. B.; Kuball, M. Control of the in-plane thermal conductivity of ultra-thin nanocrystalline diamond films through the grain and grain boundary properties. *Acta Mater.* **2016**, *103*, 141−152.
(66) Sood, A.; Cheaito, R.; Bai, T.; Kwon, H.; Wang, Y.; Li, C.; Yates, L.; Bougher, T.; Graham, S.; Asheghi, M.; Goorsky, M.; Goodson, K. E. Direct Visualization of Thermal Conductivity Suppression Due to Enhanced Phonon Scattering Near Individual Grain Boundaries. *Nano Lett.* **2018**, *18*, 3466−3472.
(67) Gu, C.; Jiang, X.; Jin, Z. The preparation of high quality oriented diamond thin films via low temperature and hydrogen ion etched nucleation. *Diamond Relat. Mater.* **1999**, *8*, 262−266.
(68) Liu, T.; Raabe, D.; Mao, W.-M. A review of crystallographic textures in chemical vapor-deposited diamond films. *Front. Mater. Sci. China* **2010**, *4*, 1−16.
(69) Smereka, P.; Li, X.; Russo, G.; Srolovitz, D. J. Simulation of faceted film growth in three dimensions: microstructure, morphology and texture. *Acta Mater.* **2005**, *53*, 1191−1204.
(70) Dong, H.; Wen, B.; Melnik, R. Relative importance of grain boundaries and size effects in thermal conductivity of nanocrystalline materials. *Sci. Rep.* **2014**, *4*, 7037.

DOI: 10.1021/acsami.9b02234
ACS Appl. Mater. Interfaces 2019, 11, 18517−18527

Supporting Information

Tunable Thermal Energy Transport across Diamond Membranes and Diamond-Si Interfaces by Nanoscale Graphoepitaxy

Zhe Cheng, Tingyu Bai, Jingjing Shi, Tianli Feng, Yekan Wang, Matthew Mecklenburg, Chao Li, Karl D. Hobart, Tatyana I. Feygelson, Marko J. Tadjer*, Bradford B. Pate, Brian M. Foley, Luke Yates, Sokrates T. Pantelides, Baratunde A. Cola, Mark Goorsky, Samuel Graham*

[1] George W. Woodruff School of Mechanical Engineering, Georgia Institute of Technology, Atlanta, Georgia 30332, USA

[2] Materials Science and Engineering, University of California, Los Angeles, Los Angeles, CA, 91355, USA

[3] Department of Physics and Astronomy and Department of Electrical Engineering and Computer Science, Vanderbilt University, Nashville, Tennessee 37235, USA

[4] Materials Science and Technology Division, Oak Ridge National Laboratory, Oak Ridge, Tennessee 37831, USA

[5] Core Center of Excellence in Nano Imaging (CNI), University of Southern California, Los Angeles, California 90089, USA

[6] U.S. Naval Research Laboratory, 4555 Overlook Ave SW, Washington, DC 20375, USA

[7] School of Materials Science and Engineering, Georgia Institute of Technology, Atlanta, Georgia 30332, USA

* Corresponding authors: sgraham@gatech.edu; karl.hobart@nrl.navy.mil

Figure S1 shows the structure of the patterns. Figure S1 (a-c) shows the cross-section SEM images of the patterned trenches. The average top width, bottom width, and height of the trenches for Sample A1 are 60 nm, 77 nm, and 47 nm, respectively. Figure S1 (d) shows the schematic diagram of the patterned trenches.

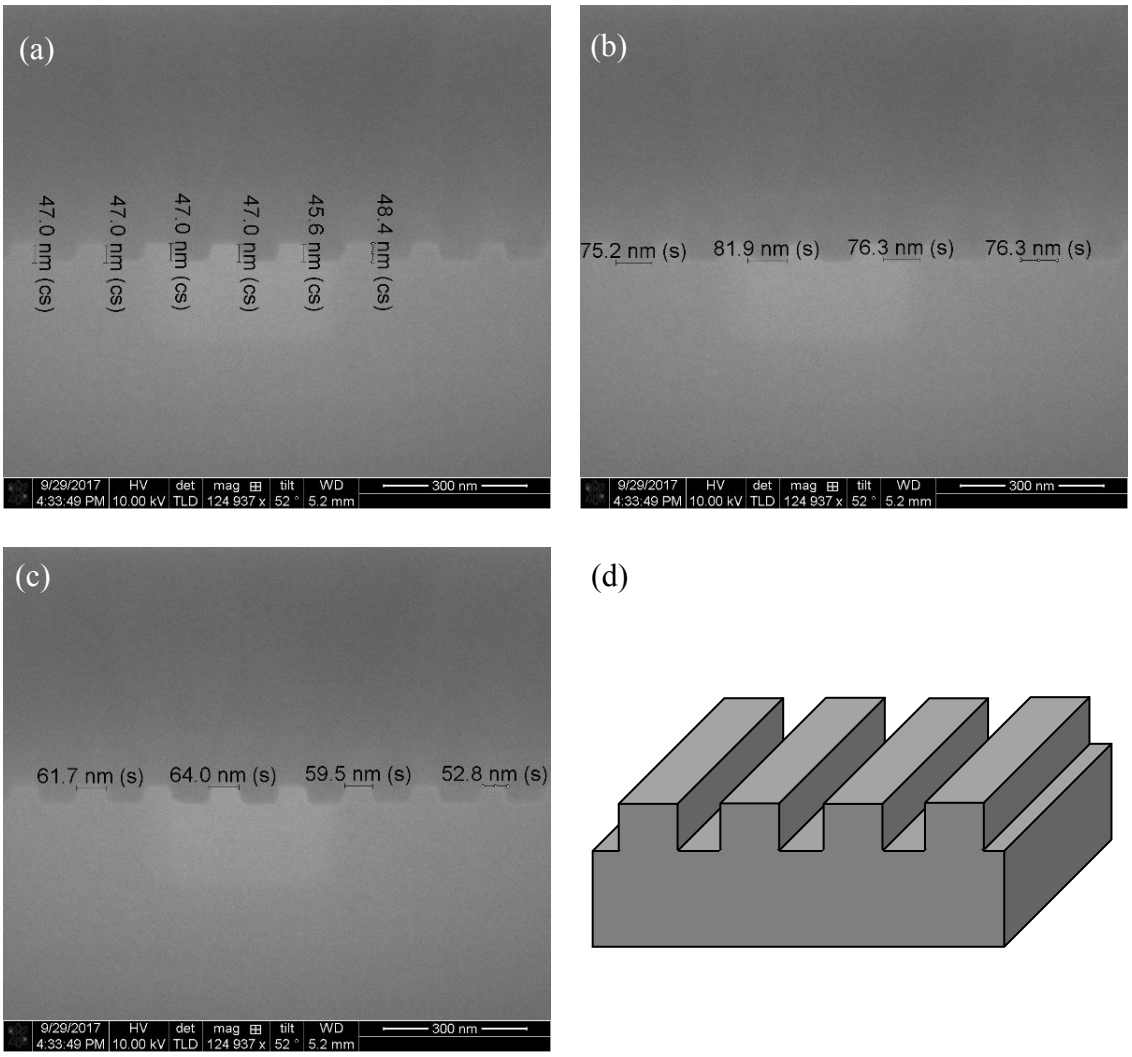

Figure S1. (a-c) Cross-section SEM images of the patterned trenches. (d) Schematic diagram of the patterned trenches. The average height, top and bottom dimensions of the trench structure are 47 nm, 60 nm, and 77 nm, respectively.

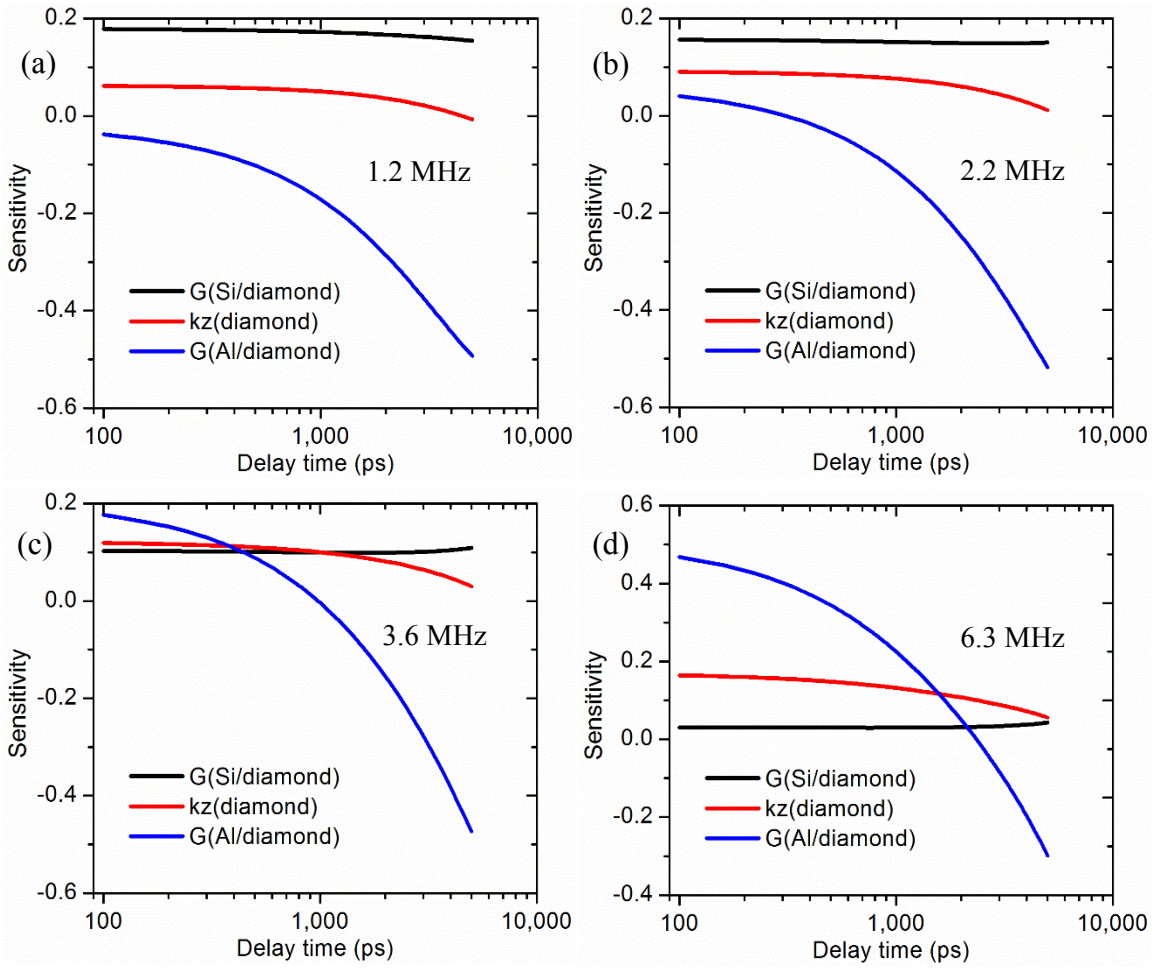

Figure S2. TDTR Sensitivity of silicon-diamond TBC, diamond cross-plane thermal conductivity, diamond-Al TBC with different modulation frequencies (1.2-6.3 MHz).

For normal single frequency TDTR measurements on a two-layer sample (Al layer and sample layer), two free parameters are fitted (Al-sample TBC and sample thermal conductivity). But for three layer samples (Al layer, diamond layer, and silicon layer), there are three free parameters (Al-diamond TBC, diamond thermal conductivity, and diamond-silicon TBC). One single frequency measurement is not enough to fit for three free parameters. The TDTR modulation frequency determines the thermal penetration depth into the samples. Low frequency TDTR measurements penetrate deeply into the samples, resulting in large sensitivity of the buried

interface TBC (diamond-silicon TBC). High frequency TDTR measurements penetrate less deeply, resulting in large sensitivity of parameters close to the sample surface (large sensitivity of diamond thermal conductivity and small sensitivity of the diamond-silicon TBC). Both frequencies have large sensitivity to Al-diamond TBC. That's why we need to use multi-frequency measurements on the same spot to fit for both diamond thermal conductivity and diamond-silicon TBC.

The definition of TDTR sensitivity is

$$S_i = \frac{\partial \ln\left(-V_{in}/V_{out}\right)}{\partial \ln(p_i)} \qquad \text{(Equation S1)}$$

Where S_i is the sensitivity to parameter i, $-V_{in}/V_{out}$ is the TDTR signal, p_i is the value of parameter i. Figure S2 shows the sensitivity of the three unknown parameters (Al-diamond TBC, diamond cross-plane thermal conductivity, diamond-silicon TBC) change with delay time. The larger absolute value of the sensitivity is, the more sensitive to that parameter the TDTR signal is. The sensitivity of Al-diamond TBC is very large for every frequency. The sensitivity of diamond cross-plane thermal conductivity increases with modulation frequency. At high frequency, heat only penetrates into the diamond layer, the TDTR signal is more sensitive to thermal conductivity of the diamond layer. At low frequency, heat penetrates through the silicon-diamond interface, resulting in relatively large sensitivity to the silicon-diamond TBC. Because the thermal resistance of the silicon-diamond interface is larger than that of the diamond layer, the sensitivity of diamond thermal conductivity decreases at low frequencies. To fit for three unknown parameters, we use three frequency TDTR measurements (1.2-3.6 MHz or 2.2-6.3 MHz) because 1.2 MHz and 2.2 MHz are sensitive to diamond-silicon TBC while 3.6 MHz and 6.3 MHz are sensitive to diamond cross-plane thermal conductivity. The modulation frequencies are selected according to the sample structure and thermal properties.

The TDTR experimental data is fitted with an analytical solution to obtain unknown parameters. The step-by-step derivation of this analytical solution can be found in references.[1-3] In the analytical solution, each layer involves three parameters (thermal conductivity, volumetric heat capacity, thickness). The thermal boundary conductance of the interfaces are unknown. In our scenario, we have three layers (silicon, diamond, and Al). For the bulk silicon substrate, we can find all thermal properties from literature (thermal conductivity, specific heat, and density). The thickness of the silicon substrate is not important because the substrate is thermally thick for TDTR measurements. The volumetric heat capacity and thickness of the diamond layer can be found in literature or measured by SEM. The volumetric heat capacity of Al is from literature and the thickness is measured by picosecond acoustic method during TDTR measurements.[4] There are only three unknown parameters in the analytical solution: cross-plane thermal conductivity of diamond, diamond-silicon interface conductance, and diamond-Al interface conductance. We measured the same spot on a sample with three different modulation frequencies, which have different sensitivities for these three parameters.

In terms of the parameters used in the TDTR data fitting, the thickness of Al and diamond layers are measured with the picosecond-acoustic method and SEM. The thermal conductivity of Al layer is determined by measuring its electrical conductivity and applying the Wiedemann-Franz law. The diamond in-plane thermal conductivity is fixed as 120 W/m-K for Sample A2, B2, and ref2 according to our previous results and its sensitivity to TDTR signal is small.[5] The corresponding anisotropic ratio of thermal conductivity is reasonable as well.[6] All the other parameters are from

literatures.[7-10] Figure S3 shows typical multi-frequency TDTR fitting curves. The experimental data (circles) and theoretical fitting data (lines) have excellent agreement.

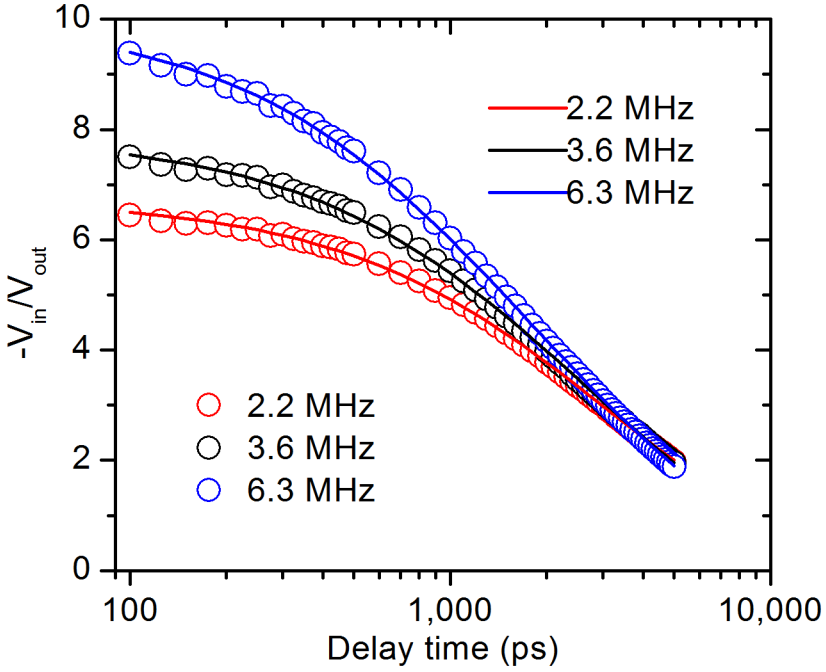

Figure S3. Typical multi-frequency TDTR fitting curves. The circles are experimental data and the lines are theoretical fitting data.

Figure S4 is a schematic diagram of the TEM sample preparation using the FIB. For plan view samples, the whole sample was mount in the FIB vertically. Next, the ion beam was used to thin the sample. One portion of the sample is thinned such that only an electron transparent layer made up of grains near the surface are present. The other portion was thinned such that only an electron transparent layer of diamond near the interface remains. Then this sample was studied using TEM to produce plan-view TEM images at both the near surface side and interface side in close proximity to each other. The plan-view images are used for grain size measurements. The cross-

section TEM sample is prepared with the same method but with the sample mounted horizontally in the FIB.

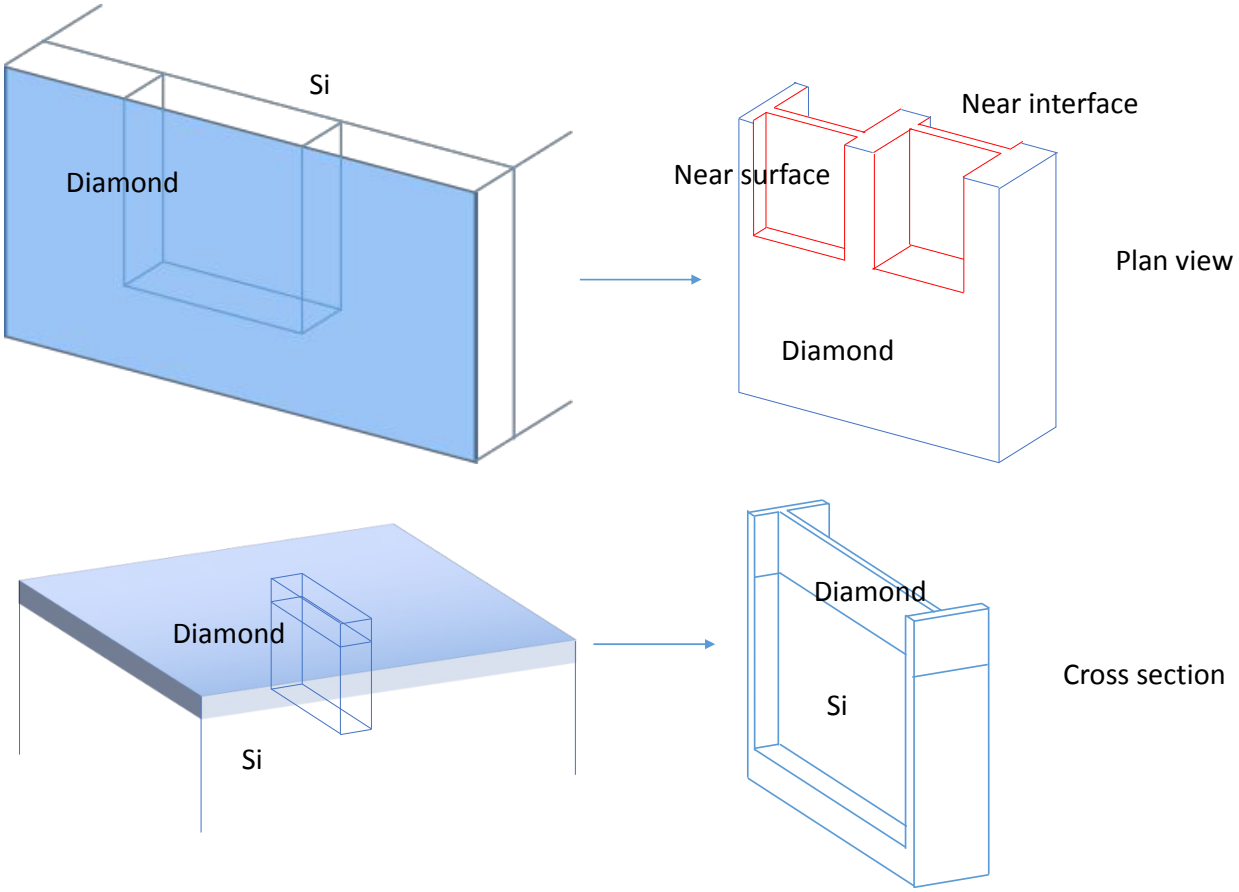

Figure S4. Schematic diagram of TEM sample preparation.

REFERENCES

(1) Cahill, D. G. Analysis of heat flow in layered structures for time-domain thermoreflectance. *Review of scientific instruments* **2004,** *75* (12), 5119-5122.

(2) Schmidt, A. J. Pump-probe thermoreflectance. *Annual Review of Heat Transfer* **2013,** *16* (1).

(3) Feser, J. P.; Cahill, D. G. Probing anisotropic heat transport using time-domain thermoreflectance with offset laser spots. *Review of Scientific Instruments* **2012,** *83* (10), 104901.

(4) Cheng, Z.; Bougher, T.; Bai, T.; Wang, S. Y.; Li, C.; Yates, L.; Foley, B.; Goorsky, M. S.; Cola, B. A.; Faili, F. Probing Growth-Induced Anisotropic Thermal Transport in High-Quality CVD Diamond Membranes by Multi-frequency and Multi-spot-size Time-Domain Thermoreflectance. *ACS applied materials & interfaces* **2018**, 10 (5), 4808-4815.

(5) Graham, S. *Thermal Transport in Diamond Films for Electronics Thermal Management*; Georgia Institute of Technology Atlanta United States: 2018.

(6) Sood, A.; Cho, J.; Hobart, K. D.; Feygelson, T. I.; Pate, B. B.; Asheghi, M.; Cahill, D. G.; Goodson, K. E. Anisotropic and inhomogeneous thermal conduction in suspended thin-film polycrystalline diamond. *Journal of Applied Physics* **2016,** *119* (17), 175103.

(7) Asheghi, M.; Touzelbaev, M.; Goodson, K.; Leung, Y.; Wong, S. Temperature-dependent thermal conductivity of single-crystal silicon layers in SOI substrates. *Journal of Heat Transfer* **1998,** *120* (1), 30-36.

(8) Bougher, T. L.; Yates, L.; Lo, C.-F.; Johnson, W.; Graham, S.; Cola, B. A. Thermal boundary resistance in GaN films measured by time domain thermoreflectance with robust Monte Carlo uncertainty estimation. *Nanoscale and Microscale Thermophysical Engineering* **2016,** *20* (1), 22-32.

(9) Yates, L.; Sood, A.; Cheng, Z.; Bougher, T.; Malcolm, K.; Cho, J.; Asheghi, M.; Goodson, K.; Goorsky, M.; Faili, F. Characterization of the Thermal Conductivity of CVD Diamond for GaN-on-Diamond Devices, *Compound Semiconductor Integrated Circuit Symposium (CSICS)*, 2016 IEEE, IEEE: 2016; pp 1-4.

(10) Cheaito, R.; Sood, A.; Yates, L.; Bougher, T. L.; Cheng, Z.; Asheghi, M.; Graham, S.; Goodson, K. Thermal conductivity measurements on suspended diamond membranes using picosecond and femtosecond time-domain thermoreflectance, *Thermal and Thermomechanical Phenomena in Electronic Systems (ITherm)*, 2017 16th IEEE Intersociety Conference on, IEEE: 2017; pp 706-710.